Ballistic heat transport in MoS_2 monolayers

Rutger Duflou[1,2], Michel Houssa[1,2], and Aryan Afzalian[1]
[1] *imec, Kapeldreef 75, 3001 Leuven, Belgium*
[2] *KU Leuven, Dept. of Physics and Astronomy, Celestijnenlaan 200 D, 3001 Leuven, Belgium*
rutger.duflou@imec.be

***Abstract*—Simulating phonons out of equilibrium is critical for the correct incorporation of self-heating effects in nanodevices. We extend our Non-Equilibrium Green's function transport solver, ATOMOS, to allow for the simulation of phonon transport and investigate ballistic thermal transport in a MoS_2 monolayer. We find thermal conductances that match well with previous work, both in magnitude and temperature dependency, but do not observe a significant anisotropy.**

***Index Terms*—heat transport, NEGF, 2D materials**

I. Introduction

Two-dimensional (2D) materials, characterized by their uniform, atomically thin thickness, are predicted to demonstrate excellent electrostatic control [1], [2] and reduced variability [3], [4] in next-generation devices. In the last two decades, the study of 2D materials has heavily relied on ab-initio techniques [1]. It has been shown that correct characterization of electronic transport in 2D semiconductor devices requires the incorporation of scattering due to electron-phonon interactions [5], [6]. In most work, however, the phonons are considered to be at equilibrium at a fixed temperature. This forgoes the effect of self-heating, where additional phonons are created due to electron-phonon interactions, leading to localized increases of the temperature. Previous work has shown that the incorporation of self-heating in simulations can alter the predicted device performance for silicon nanowires [7]. A major requirement for a correct assessment of the self-heating is the explicit simulation of phonons out of equilibrium to allow for heat dissipation. In this work, we extended our Non-Equilibrium Green's function (NEGF) transport solver, ATOMOS [5], to allow for the computation of heat transport characteristics in 2D materials through the explicit simulation of phonon transport. Additionally, the interatomic force constants are calculated using the Density Functional Perturbation Theory (DFPT) formalism in combination with the Perturbo code [8]. This is in contrast to the valence-force field method in a frozen phonon approach [7], which requires large supercells for the calculation of accurate phonon dispersion relations [9].

II. Methods

In this work, MoS_2 was selected due to its maturity and the abundance of experimental data available. The calculation of the thermal conductance happens in two steps. First, the electronic bands and phonon dispersion relations are calculated using the Quantum Espresso [10] Density Functional Theory (DFT) code. These states are then converted to a localized basis set, i.e., Wannier functions with their corresponding Hamiltonian elements, $h_{i,j}$, using Wannier90 [11], and interatomic force constants, $k_{i,j}$, using Perturbo, for electrons and phonons, respectively. Finally, these Hamiltonian elements and interatomic force constants are combined in the NEGF formalism by ATOMOS to compute heat currents.

Funded by the FWO as part of the PhD fellowship 1100321N

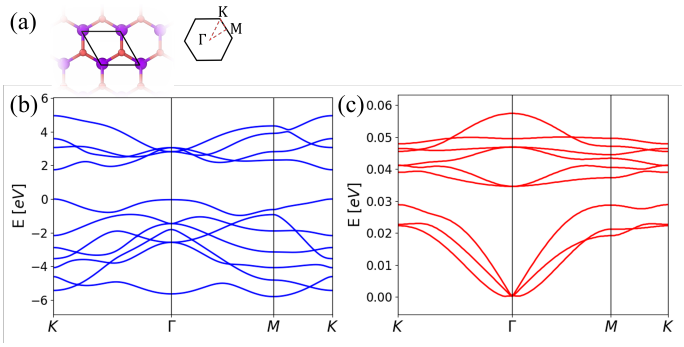

Fig. 1. The material characteristics of MoS_2. (a) shows the crystal structure, the corresponding Brillouin zone and its high-symmetry points. (b) and (c) shows the electronic band structure and phonon dispersion relation, respectively.

A. DFT

The crystal was relaxed with convergence criteria of less than 10^{-16} Ry energy variation between two self-consistent field (scf) iterations and less than 5.0×10^{-6} Ry/Bohr for the forces and 5.0×10^{-7} Ry for the energy variation between two geometry optimization steps. The PBE exchange-correlation functional was used with ultrasoft pseudopotentials and the Grimme DFT-D3 van der Waals correction was used during relaxation. A 20 Å vacuum was inserted between layers with truncation of the Coulomb interaction in the z-direction. A $16 \times 16 \times 1$ Monkhorst-Pack grid was used and the energy cutoff for the plane wave basis was set to 70 Ry. Both the k-grid density and cutoff were obtained through a convergence test, leading to an estimated relative error on the energy of 10^{-6} and on the lattice constant of 10^{-4}. The obtained electronic bands and phonon dispersion relations were converted to a localized basis set using Wannier90 and Perturbo, respectively. 5 d and 3 p orbitals were used as initial guesses for the Wannier functions on Mo and S, respectively, during the Wannierization process. The obtained electronic bands and phonon dispersion relations are shown in Figure 1.

B. NEGF

ATOMOS uses the matrix elements to compute a device Hamiltonian and dynamical matrix, H and K, respectively, where

$$K_{i,j} = \frac{k_{i.j}}{\sqrt{m_i m_j}}. \tag{1}$$

The electron and phonon Green's functions are then given by [7]

$$G = (E + i\eta - H - \Sigma)^{-1} \tag{2}$$
$$G^{\lessgtr} = G\Sigma^{\lessgtr}G^{\dagger} \tag{3}$$
$$D = (\hbar^2\omega^2 + i\eta - K - \Pi)^{-1} \tag{4}$$
$$D^{\lessgtr} = D\Pi^{\lessgtr}D^{\dagger} \tag{5}$$

where G (D) is the electron (phonon) retarded Green's function, $G^{\dagger}$ ($D^{\dagger}$) is its Hermitian conjugate, the advanced Green's function, and $G^{<}$ ($D^{<}$) and $G^{>}$ ($D^{>}$) are the electron (phonon) lesser and greater Green's function. Σ (Π) is the electron (phonon) self-energy due to injection at the contacts. Contributions to the self-energies due to electron-phonon coupling are neglected, implying that our simulations are ballistic. The electronic and phononic contributions to the heat current are calculated from these Green's functions as [7]

$$J_{el,i\to j} = \frac{2}{\hbar}\int_{-\infty}^{+\infty} E(h_{i,j}G^{<}_{j,i} - h_{j,i}G^{<}_{i,j})\frac{dE}{2\pi}, \tag{6}$$
$$J_{ph,i\to j} = \hbar\int_{-\infty}^{+\infty} \omega(k_{i,j}D^{<}_{j,i} - k_{j,i}D^{<}_{i,j})\frac{d\omega}{2\pi}. \tag{7}$$

The device consists of a $10\,\mathrm{nm}$ long sheet of MoS_2 with transport along either the zigzag or armchair direction by application of a temperature difference. The orthogonal direction is considered periodic. The periodic boundary conditions are accommodated by Fourier transforming the device Hamiltonian and dynamical matrix to reciprocal space along the periodic direction. 10 k-points are then used to sample half of the Brillouin zone, while the other half is obtained from symmetry.

III. Results

The results on the phononic and electronic transport properties are discussed separately.

A. Phononic heat current

The results for the phononic part of the ATOMOS simulation are show in Figure 2. Figure 2(a) shows the heat current spectrum. Both the optical and acoustic phonon branches contribute, with a maximum achieved for the acoustic branches at energies of $20\,\mathrm{meV}$. Figure 2(b) demonstrates how the heat flux increases linearly with the temperature difference, allowing for the extraction of a value for the thermal conductance. The thermal conductance as a function of temperature is shown in Figure 2(c). At room temperature, the thermal conductance

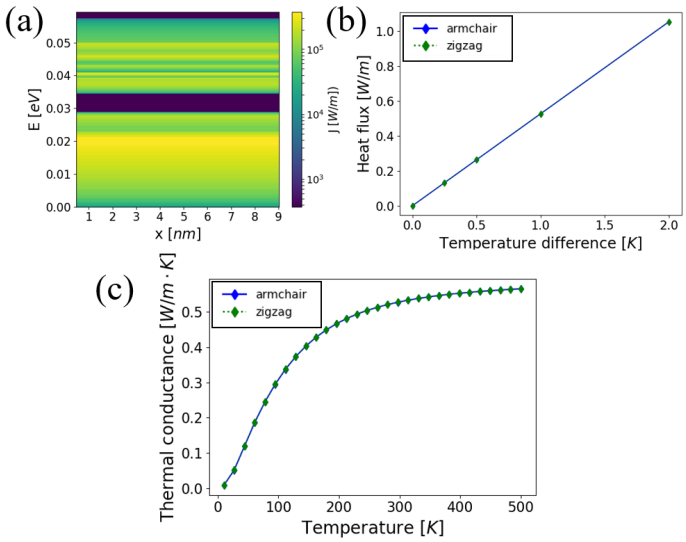

Fig. 2. Phononic heat transport results. (a) shows the phononic heat current spectrum at 300 K for a temperature difference of 1 K. (b) shows the integrated heat flux per nanometer at 300 K for several applied temperature differences. (c) shows the extracted thermal conductance at different temperatures.

is found to be $0.527\,\mathrm{W\,m^{-1}\,K^{-1}}$. The results are in good agreement with those reported in [12]. The trend of the thermal conductance as a function of temperature is very similar and applying the same transformation for the calculation of the thermal conductivity as in [12], namely

$$\kappa = \sigma L/h \tag{8}$$

with $L = 1\,\mu\mathrm{m}$ and $h = 6.033\,\text{Å}$, results in a thermal conductivity of $\kappa = 878\,\mathrm{W\,m^{-1}\,K^{-1}}$, which corresponds nicely to the value of $\kappa = 841\,\mathrm{W\,m^{-1}\,K^{-1}}$ found in [12] for transport along the zigzag direction. It should be noted that, in contrast to the results in [12], our results do not show any dependency on the sheet orientation. This could be attributed to us simulating periodic sheets, while the focus in [12] lies on nanoribbons.

B. Electronic heat current

The energy of the electronic states in the material depends on the potential. Imposing a potential shift on both terminals in the NEGF simulation leaves the physics of the heat transport unchanged. The result of (6), however, does depend on this arbitrary potential shift. We propose two workarounds. The first approach consists of normalizing the energies compared to a reference energy that shifts with the potential in the terminals, e.g., the Fermi energy:

$$J_{el,i\to j} = \frac{2}{\hbar}\int_{-\infty}^{+\infty} (E - E_F)(h_{i,j}G^{<}_{j,i} - h_{j,i}G^{<}_{i,j})\frac{dE}{2\pi}. \tag{9}$$

The second approach relies on the fact that this ambiguity only arises for systems with a nonzero current. However, the Seebeck effect can have the effect of creating a counter

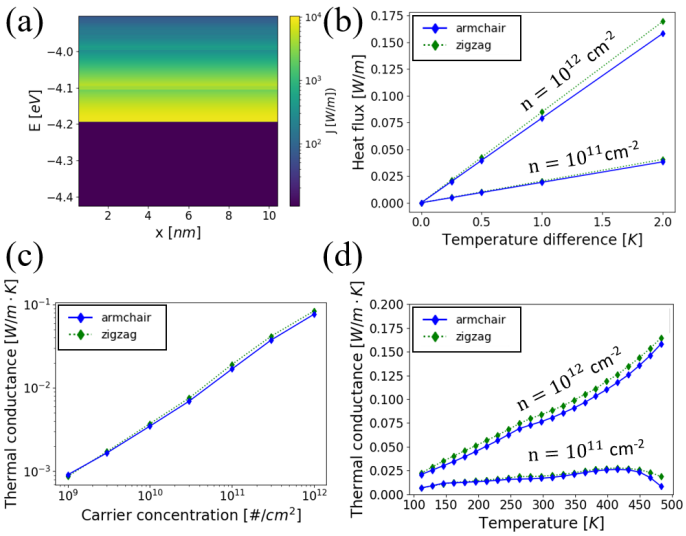

Fig. 3. Electronic heat transport results for energy normalization. (a) shows the electronic heat current spectrum at 300 K for a temperature difference of 1 K and an armchair transport direction. (b) shows the integrated heat flux per nanometer at 300 K for several applied temperature differences both for a carrier concentration of $1 \times 10^{11}\,\mathrm{cm}^{-2}$ and $1 \times 10^{12}\,\mathrm{cm}^{-2}$, respectively. (c) shows the extracted thermal conductance at 300 K at different carrier concentrations. (d) shows the extracted thermal conductance at different temperatures for a carrier concentration of $1 \times 10^{11}\,\mathrm{cm}^{-2}$ and $1 \times 10^{12}\,\mathrm{cm}^{-2}$, respectively.

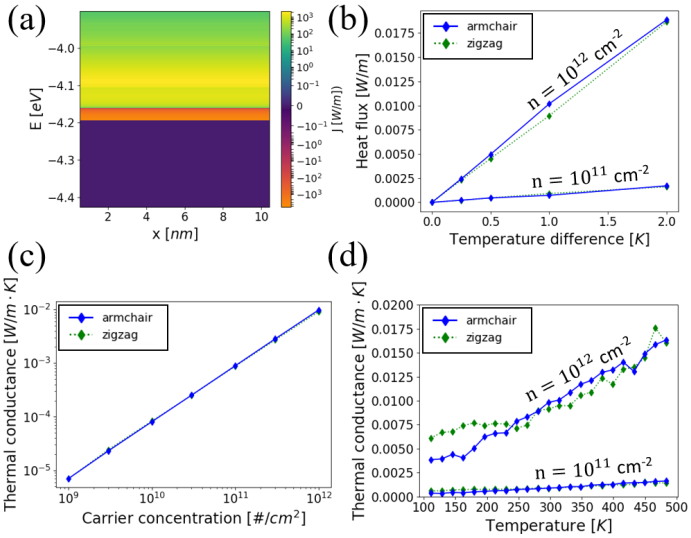

Fig. 4. Electronic heat transport results for zero net current due to the Seebeck effect. (a) shows the electronic heat current spectrum at 300 K for a temperature difference of 1 K and an armchair transport direction. (b) shows the integrated heat flux per nanometer at 300 K for several applied temperature differences both for a carrier concentration of $1 \times 10^{11}\,\mathrm{cm}^{-2}$ and $1 \times 10^{12}\,\mathrm{cm}^{-2}$, respectively. (c) shows the extracted thermal conductance at 300 K at different carrier concentrations. (d) shows the extracted thermal conductance at different temperatures for a carrier concentration of $1 \times 10^{11}\,\mathrm{cm}^{-2}$ and $1 \times 10^{12}\,\mathrm{cm}^{-2}$, respectively.

electromotive force (emf), reducing the net current, possibly eliminating it completely.

The results for the first approach are shown in Figure 3. Figure 3(a) shows the heat current spectrum. Figure 3(b) demonstrates how the heat flux increases linearly with the temperature difference, allowing for the extraction of a value for the thermal conductance. However, the heat flux, and hence, the conductance, depend on the carrier concentration as demonstrated in Figure 3(c). At theoretically predicted intrinsic carrier concentrations ($\sim 1 \times 10^{6}\,\mathrm{cm}^{-2}$ [13]) the electronic thermal conductance is significantly lower than the phononic contribution. Extrapolating the curve in Figure 3(c), the electronic thermal conductance is predicted to exceed the phononic thermal conductance at 300 K for carrier concentrations above $2 \times 10^{13}\,\mathrm{cm}^{-2}$. The thermal conductance as a function of temperature is shown in Figure 3(d). At high carrier concentrations, the thermal conductance increases monotonically with the temperature. For lower carrier concentrations, the thermal conductance increases with temperature up to a certain value after which it decreases again. At this temperature, having a fixed carrier concentration requires a lowering of the Fermi level deeper into the band gap. This appears to give rise to a lowering of the thermal conductance. At all temperatures and carrier concentrations, a minor dependency on the orientation of the MoS_2 sheet can be observed, but it appears insignificant in comparison with other parameters such as the temperature and the carrier concentration.

Figure 4 shows the results for the second approach, where a bias over the material is imposed due to the Seebeck effect to eliminate the net current. Figure 4(a) shows the heat current spectrum. The zero net current is imposed by a bias in the systems that causes a backwards current at low energy and a forward current at high energy. The difference in energy of these currents causes a net heat current despite the zero net current. Figure 4(b) demonstrates that, similar to Figure 3(b), the heat flux increases linearly with the temperature difference and is dependent on the carrier concentration. For the carrier concentrations demonstrated here, the heat fluxes, and hence the thermal conductances, are significantly lower than for the first approach in Figure 3(b). This is expected as the backwards current at low energy in Figure 4(a) reduces the heat current, despite not eliminating it completely. Figure 4(c) shows the extracted thermal conductance as a function of the carrier concentration. Comparing to Figure 3(c), a stronger carrier concentration dependency can be observed with the Seebeck effect than without. Extrapolating the curve in Figure 4(c), the electronic thermal conductance with imposed zero net current is predicted to exceed the phononic contributions at 300 K for carrier concentrations above $6 \times 10^{13}\,\mathrm{cm}^{-2}$, i.e., higher than when no zero net current is imposed. The thermal conductance as a function of temperature is shown in Figure 4(d). The thermal conductance increases with the temperature for both of the shown carrier concentrations. The curves do not show a decrease at high temperature and low carrier concentrations such as observed in Figure 3(d). However, the thermal conductances do not increase monotonically due to noise superimposed on the curves. This noise is the result of the iterative search of the bias to obtain a net zero current. This bias is searched in an iterative way for every energy

and carrier concentration by setting the current to zero. This current is computed as the difference between two integrated quantities, i.e., the forward current at high energy and the backward current at low current, which are both affected by an integration error. The subtraction of large, nearly equal quantities affected by errors is a numerically ill-conditioned problem. The obtained biases will therefore not be perfect and the net currents will hence not be exactly zero. The large difference in the thermal conductance with and without the Seebeck effect demonstrates that any net current has a large influence on the thermal conductance. Hence, having a net current that is not perfectly zero introduces large errors on the thermal conductances in Figure 4(d).

IV. Conclusion

We used our NEGF transport solver, ATOMOS, to calculate the thermal conductance for MoS_2 nanosheets, resulting in a phononic thermal conductance of $0.527\,\mathrm{W\,m^{-1}\,K^{-1}}$ at 300 K, which corresponds well with values found in the literature. Contrary to previous work, the phononic thermal conductivity does not depend on the orientation of the nanosheet, which can possibly be attributed to a continuous sheet being simulated, i.e., periodic in the orthogonal direction, instead of nanoribbons. The electronic thermal conductance depends on the carrier concentration and on whether a nonzero net current is allowed. In both cases, the electronic thermal conductance is significantly lower than the phononic thermal conductance for intrinsic carrier concentrations. When a nonzero net current is allowed, a predicted carrier concentration of $2 \times 10^{13}\,\mathrm{cm^{-2}}$ is required to obtain a electronic thermal conductance equal to the phononic thermal conductance at 300 K. When the net current is eliminated by the Seebeck effect, the electronic thermal conductance is found to be lower for the same carrier concentration and a predicted carrier concentration of $6 \times 10^{13}\,\mathrm{cm^{-2}}$ is required to obtain a electronic thermal conductance equal to the phononic thermal conductance at 300 K. The orientation dependency of the electronic thermal conductance is larger than that of the phononic thermal conductance, but it is still insignificant compared to other parameters such as the termperature and the carrier concentration.

References

[1] F. Schwierz, J. Pezoldt, and R. Granzner, "Two-dimensional materials and their prospects in transistor electronics," *Nanoscale*, vol. 7, no. 18, pp. 8261–8283, 2015.

[2] D. Logoteta, Q. Zhang, and G. Fiori, "What can we really expect from 2d materials for electronic applications?," in *72nd Device Research Conference*, IEEE, 2014.

[3] M. Chhowalla, D. Jena, and H. Zhang, "Two-dimensional semiconductors for transistors," *Nature Reviews Materials*, vol. 1, no. 11, p. 16052, 2016.

[4] J. Kang, W. Cao, X. Xie, D. Sarkar, W. Liu, and K. Banerjee, "Graphene and beyond-graphene 2d crystals for next-generation green electronics," in *Micro-and Nanotechnology Sensors, Systems, and Applications VI*, vol. 9083, p. 908305, International Society for Optics and Photonics, 2014.

[5] A. Afzalian, "Ab initio perspective of ultra-scaled CMOS from 2d-material fundamentals to dynamically doped transistors," *npj 2D Materials and Applications*, vol. 5, no. 1, 2021.

[6] R. Duflou, M. Houssa, and A. Afzalian, "Electron-phonon scattering in cold-metal contacted two-dimensional semiconductor devices," in *2021 International Conference on Simulation of Semiconductor Processes and Devices (SISPAD)*, pp. 94–97, 2021.

[7] R. Rhyner and M. Luisier, "Atomistic modeling of coupled electron-phonon transport in nanowire transistors," *Phys. Rev. B*, vol. 89, p. 235311, Jun 2014.

[8] J.-J. Zhou, J. Park, I.-T. Lu, I. Maliyov, X. Tong, and M. Bernardi, "Perturbo: A software package for ab initio electron–phonon interactions, charge transport and ultrafast dynamics," *Computer Physics Communications*, vol. 264, p. 107970, 2021.

[9] F. Giustino, "Electron-phonon interactions from first principles," *Reviews of Modern Physics*, vol. 89, Feb 2017.

[10] P. Giannozzi, S. Baroni, N. Bonini, M. Calandra, R. Car, C. Cavazzoni, D. Ceresoli, G. L. Chiarotti, M. Cococcioni, I. Dabo, A. D. Corso, S. de Gironcoli, S. Fabris, G. Fratesi, R. Gebauer, U. Gerstmann, C. Gougoussis, A. Kokalj, M. Lazzeri, L. Martin-Samos, N. Marzari, F. Mauri, R. Mazzarello, S. Paolini, A. Pasquarello, L. Paulatto, C. Sbraccia, S. Scandolo, G. Sclauzero, A. P. Seitsonen, A. Smogunov, P. Umari, and R. M. Wentzcovitch, "QUANTUM ESPRESSO: a modular and open-source software project for quantum simulations of materials," *Journal of Physics: Condensed Matter*, vol. 21, no. 39, p. 395502, 2009.

[11] N. Marzari, A. A. Mostofi, J. R. Yates, I. Souza, and D. Vanderbilt, "Maximally localized wannier functions: Theory and applications," *Reviews of Modern Physics*, vol. 84, no. 4, pp. 1419–1475, 2012.

[12] J.-W. Jiang, X. Zhuang, and T. Rabczuk, "Orientation dependent thermal conductance in single-layer MoS2," *Sci. Rep.*, vol. 3, no. 1, p. 2209, 2013.

[13] X. Y. Ma, "Study of the electrical properties of monolayer mos2 semiconductor," in *Advanced Materials Research*, vol. 651, pp. 193–197, Trans Tech Publ, 2013.